Fast automatic wave-equation migration velocity analysis using encoded simultaneous sources

Yaxun Tang

ABSTRACT

I present a method based on source encoding for fast wave-equation migration velocity analysis (WEMVA). Instead of migrating each impulsive-source gather separately, I assemble all gathers together and migrate only one super shot gather. This procedure results in the computational cost of WEMVA to be independent from the number of impulsive-source gathers, which is typically huge for large surveys. The proposed encoding method can be applied to data acquired from any acquisition geometry, such as land or marine acquisition geometries. The velocity inversion is done automatically by solving a nonlinear optimization problem that maximizes the image stack power, which is shown to be equivalent to the data-domain inversion using only primary reflections. Preliminary results show that WEMVA with encoded sources can produce inversion results similar to those produced by conventional separate-source WEMVA, but with drastically reduced computational cost.

INTRODUCTION

Accurate reflectivity imaging requires an accurate background velocity model. As seismic exploration moves towards structurally complex areas, wave-equation migration velocity analysis (WEMVA) that better models band-limited wave phenomena becomes necessary for high-quality velocity model building. WEMVA, however, is still expensive for industrial-scale applications (Biondi and Sava, 1999; Shen et al., 2005; Albertin et al., 2006; Fei et al., 2009), both because the method uses expensive wavefield modeling engines, and because the computation needs to be carried out for each shot, resulting in a cost proportional to the number of sources, which is huge for large surveys.

Source encoding has been used in both seismic acquisition (Beasley et al., 1998; Beasley, 2008; Hampson et al., 2008; Berkhout, 2008; Tang and Biondi, 2009) and processing (Romero et al., 2000; Whitmore, 1995; Zhang et al., 2005; Liu et al., 2006; Krebs et al., 2009) to reduce the cost. The idea is that instead of firing one impulsive source at a time, we fire all encoded impulsive sources simultaneously for acquisition or/and processing. By doing so, the acquisition or/and processing effort is reduced to just one super areal shot gather instead of many impulsive source gathers, significantly reducing the acquisition or/and processing cost. In this paper, I mainly

focus on applying the source-encoding method to seismic processing, hence I assume that the data are acquired using conventional impulsive separate sources without any overlaps.

Source encoding has been widely used in migration processing, where random-phase encoding and plane-wave-phase encoding are the most popular encoding schemes. The random-phase-encoding migration, however, has had limited success. This is because the more shots randomly encoded together, the more crosstalk present in the migration image. Consequently, images obtained with many realizations need to be computed and stacked in order to attenuate the crosstalk (Romero et al., 2000). Plane-wave phase-encoding migration, on the other hand, has wider applications than random phase-encoding migration. This is because plane-wave phase-encoding function has good properties in terms of converging to a Dirac delta function (Liu et al., 2006). However, multiple plane waves need to be synthesized and migrated to remove the crosstalk artifacts. As a result, source encoding in migration can usually achieve a cost reduction by a factor of about 10 or less.

As opposed to seismic migration processing, source encoding (especially random phase encoding) seems to be more effective in seismic inversion processing, such as least-squares migration (Tang and Biondi, 2009; Dai and Schuster, 2009; Dai et al., 2010) and full waveform inversion (Krebs et al., 2009; Tang and Lee, 2010; Ben-Hadj-Ali et al., 2011). The key element in encoded simultaneous-source inversion is the regeneration of random codes at each iteration (Krebs et al., 2009; Tang and Lee, 2010; Dai et al., 2010; Ben-Hadj-Ali et al., 2011). Different sets of random codes at each iteration enable destructive summation of the crosstalk over iterations, and consequently the residual crosstalk in the inverted model is gradually removed as inversion proceeds. Encoded simultaneous-source inversion operates on one super shot gather instead of many impulsive-source gathers at each iteration, therefore the computational cost is independent of the number of sources. Although more or less counter-intuitive, Krebs et al. (2009) have reported that encoded simultaneous-source inversion has a similar convergence rate compared to separate-source inversion. As a result, source encoding in inversion can achieve a cost reduction by a factor of the number of sources, which can be significant for large surveys.

One commonality of the above mentioned inversion processing (least-squares migration and full waveform inversion) is the minimization of a data-domain objective function, which compares the differences between the modeled and the observed data. The difference-based objective function, however, restricts the application of encoded simultaneous-source inversion to only data acquired with a fixed receiver spread, such as in land or ocean bottom cable (OBC) acquisition geometries (Krebs et al., 2009). This is because modeling using encoded simultaneous sources implicitly assumes that each receiver listens to all shots. This is obviously not the case for marine acquisition geometries, where the towed receiver spread moves along with the sources. The mismatch in acquisition is irreconcilable and will cause wrong model updates.

In this paper, I apply the source-encoding method to WEMVA, which optimizes an objective function formulated in the image domain instead of the data domain.

In particular, I optimize the velocity by maximizing the image stack power (or minimizing its negative). I will show that the objective function to maximize (or minimize) is based on the crosscorrelation between the source and receiver wavefields, and that source encoding can be applied to arbitrary acquisition geometries, regardless of whether or not the receiver spread is fixed. Similar to the data-domain multi-source inversion, encoded simultaneous-source WEMVA also generates gradients contaminated by crosstalk. Therefore, regeneration of random codes at each iteration becomes necessary to mitigate the impact of crosstalk on velocity updates.

In the subsequent sections, I first review the theory of WEMVA based on image-stack-power maximization (or equivalently negative image-stack-power minimization). I prove that minimizing the negative image stack power is equivalent to the data domain Born wavefield inversion, which minimizes the difference between the modeled and observed primary reflections. I then show how source encoding can be applied to WEMVA. Finally, I apply both separate-source WEMVA and encoded simultaneous-source WEMVA to invert a truncated Marmousi model.

THEORY

I pose the velocity estimation problem as an optimization problem that tries to maximize the image stack power across the reflection angle, taking advantage of the fact that seismic events should be aligned and hence most constructively stacked in the angle domain, if migrated using an accurate velocity model (Soubaras and Gratacos, 2007). Instead of solving it as a maximization problem, I actually solve it as a minimization problem that minimizes the negative image stack power. Because the reflection-angle stacked section is equivalent to the zero-subsurface offset image, the objective function that I use to minimize is therefore defined as follows:

$$J = -\frac{1}{2}\sum_{\mathbf{x}} m^2_{\text{mig}}(\mathbf{x}), \tag{1}$$

where $m_{\text{mig}}(\mathbf{x})$ is the zero-subsurface-offset image at image point $\mathbf{x} = (x, y, z)$, obtained by crosscorrelating the forward propagated source wavefield with the backward propagated receiver wavefield as follows:

$$m_{\text{mig}}(\mathbf{x}) = \sum_{\mathbf{x}_s}\sum_{\omega} S(\mathbf{x}, \mathbf{x}_s, \omega) R(\mathbf{x}, \mathbf{x}_s, \omega), \tag{2}$$

where $S(\mathbf{x}, \mathbf{x}_s, \omega)$ and $R(\mathbf{x}, \mathbf{x}_s, \omega)$ are the source and receiver wavefield at image point $\mathbf{x}$, respectively, for a source located at $\mathbf{x}_s = (x_s, y_s, 0)$ and at angular frequency ω. If a one-way extrapolator is used, S and R satisfy the following one-way wave equations:

$$\begin{cases} \left(\frac{\partial}{\partial z} + i\sqrt{\frac{\omega^2}{v^2(\mathbf{x})} + \nabla^2}\right) S(\mathbf{x}, \mathbf{x}_s, \omega) = 0 \\ S(x, y, z = 0, \mathbf{x}_s, \omega) = \delta(x - x_s, y - y_s) f^*_s(\omega) \end{cases}, \tag{3}$$

and

$$\begin{cases} \left(\frac{\partial}{\partial z} + i\sqrt{\frac{\omega^2}{v^2(\mathbf{x})} + \nabla^2}\right) R(\mathbf{x}, \mathbf{x}_s, \omega) = 0 \\ R(x, y, z = 0, \mathbf{x}_s, \omega) = Q(x, y, \mathbf{x}_s, \omega) \end{cases}, \tag{4}$$

where * denotes taking the adjoint; $v(\mathbf{x})$ is the velocity at image point $\mathbf{x}$; $f_s(\omega)$ is the source signature; $\delta(\cdot)$ is the Dirac delta function; $\nabla^2 = \frac{\partial^2}{\partial x^2} + \frac{\partial^2}{\partial y^2}$ is the Laplacian operator. Q is the observed data mapped onto the computation grid, which is defined as follows:

$$Q(x, y, \mathbf{x}_s, \omega) = \sum_{\mathbf{x}_r} W(\mathbf{x}_r, \mathbf{x}_s)\delta(x - x_r, y - y_r)d_{\text{obs}}(\mathbf{x}_r, \mathbf{x}_s, \omega), \tag{5}$$

where d_{obs} is the observed data recorded at $\mathbf{x}_r = (x_r, y_r, 0)$ due to a source at $\mathbf{x}_s$; $W(\mathbf{x}_r, \mathbf{x}_s)$ is the acquisition mask operator, which contains ones where we record data and zeros where we do not.

Since flat angle gathers generate the most coherent stack, the negative image-stack-power minimization objective function defined by equation 1 is intuitive to understand. Objective function 1, however, has an alternative interesting interpretation as shown in Appendix A, which proves that under the least-squares assumption, minimization of objective function 1 is equivalent to the data-domain Born wavefield inversion, which minimizes the differences between the modeled and observed primary reflections.

Objective function 1 is usually minimized using local optimization techniques, which require explicit calculation of the gradient. The gradient is obtained by taking the derivative of J with respect to velocity $v(\mathbf{y})$ ($\mathbf{y}$ is the velocity coordinates) as follows:

$$g(\mathbf{y}) = \frac{\partial J}{\partial v(\mathbf{y})} = -\sum_{\mathbf{x}} \frac{\partial m_{\text{mig}}(\mathbf{x})}{\partial v(\mathbf{y})} m_{\text{mig}}(\mathbf{x}), \tag{6}$$

where the sensitivity kernel, or tomographic operator, $\frac{\partial m_{\text{mig}}(\mathbf{x})}{\partial v(\mathbf{y})}$, can be easily obtained as follows:

$$\frac{\partial m_{\text{mig}}(\mathbf{x})}{\partial v(\mathbf{y})} = \sum_{\mathbf{x}_s}\sum_{\omega}\left(\frac{\partial S(\mathbf{x}, \mathbf{x}_s, \omega)}{\partial v(\mathbf{y})} R(\mathbf{x}, \mathbf{x}_s, \omega) + S(\mathbf{x}, \mathbf{x}_s, \omega)\frac{\partial R(\mathbf{x}, \mathbf{x_s}, \omega)}{\partial v(\mathbf{y})}\right). \tag{7}$$

Note the summations over $\mathbf{x}_s$ in equations 2 and 7. This means that the computation for the image m_{mig} and the gradient g needs to be carried out for each source independently, resulting in a cost proportional to the number of sources. The gradient g is usually calculated using the adjoint-state technique without explicitly constructing the sensitivity kernel (Shen, 2004; Sava and Vlad, 2008; Tang et al., 2008).

For encoded simultaneous-source WEMVA, the objective function to be minimized is defined as follows:

$$\widetilde{J} = -\frac{1}{2}\sum_{\mathbf{x}} \widetilde{m}^2_{\text{mig}}(\mathbf{x}), \tag{8}$$

where the zero-subsurface-offset image $\widetilde{m}_{\rm mig}$ is obtained by crosscorrelating the encoded source wavefield, $\widetilde{S}$, and the encoded receiver wavefield, $\widetilde{R}$, as follows:

$$\widetilde{m}_{\rm mig}(\mathbf{x}) = \sum_{\omega} \widetilde{S}(\mathbf{x},\omega)\widetilde{R}(\mathbf{x},\omega). \tag{9}$$

The encoded source and receiver wavefields satisfy the following one-way wave equations:

$$\begin{cases} \left(\frac{\partial}{\partial z} + i\sqrt{\frac{\omega^2}{v^2(\mathbf{x})} + \nabla^2}\right)\widetilde{S}(\mathbf{x},\omega) = 0 \\ \widetilde{S}(x,y,z=0,\omega) = \sum_{\mathbf{x}_s} \delta(x-x_s, y-y_s) f_s^*(\omega)\alpha^*(\mathbf{x}_s,\omega) \end{cases}, \tag{10}$$

and

$$\begin{cases} \left(\frac{\partial}{\partial z} + i\sqrt{\frac{\omega^2}{v^2(\mathbf{x})} + \nabla^2}\right)\widetilde{R}(\mathbf{x},\omega) = 0 \\ \widetilde{R}(x,y,z=0,\omega) = \sum_{\mathbf{x}_s} Q(x,y,\mathbf{x}_s,\omega)\alpha(\mathbf{x}_s,\omega) \end{cases}, \tag{11}$$

where $\alpha(\mathbf{x}_s,\omega)$ is the phase encoding function. In this paper, I mainly focus on random phase encoding, therefore α is defined as follows:

$$\alpha(\mathbf{x}_s,\omega) = e^{i\gamma(\mathbf{x}_s,\omega)}, \tag{12}$$

where $i = \sqrt{-1}$, and $\gamma(\mathbf{x}_s,\omega)$ is a uniformly distributed random sequence from 0 to 2π. Tang (2011) shows that with this choice of random phase function, α has a zero expectation. Note that the source encoding can be applied to data recorded from arbitrary types of acquisition geometries. The simultaneous-source migrated image ($\widetilde{m}_{\rm mig}$) will always converge to the separate-source migrated image ($m_{\rm mig}$) as long as the encoding function satisfies $\alpha^*(\mathbf{x}_s,\omega)\alpha(\mathbf{x}'_s,\omega) \approx \delta(\mathbf{x}_s - \mathbf{x}'_s)$.

The gradient of objective function 8 is

$$\widetilde{g}(\mathbf{y}) = \frac{\partial \widetilde{J}}{\partial v(\mathbf{y})} = -\sum_{\mathbf{x}} \frac{\partial \widetilde{m}_{\rm mig}(\mathbf{x})}{\partial v(\mathbf{y})} \widetilde{m}_{\rm mig}(\mathbf{x}), \tag{13}$$

where the tomographic operator, $\frac{\partial \widetilde{m}_{\rm mig}(\mathbf{x})}{\partial v(\mathbf{y})}$, in the encoded-source domain is defined as follows:

$$\frac{\partial \widetilde{m}_{\rm mig}(\mathbf{x})}{\partial v(\mathbf{y})} = \sum_{\omega} \left(\frac{\partial \widetilde{S}(\mathbf{x},\omega)}{\partial v(\mathbf{y})} \widetilde{R}(\mathbf{x},\omega) + \widetilde{S}(\mathbf{x},\omega) \frac{\partial \widetilde{R}(\mathbf{x},\omega)}{\partial v(\mathbf{y})} \right). \tag{14}$$

Note that equations 9 and 14 do not have a summation over the sources. Therefore, the cost of computing the image $\widetilde{m}_{\rm mig}$ and the gradient $\widetilde{g}$ is independent of the number of sources, as opposed to the separate-source case. The gradient $\widetilde{J}$ is also calculated using the adjoint-state technique using encoded simultaneous sources (Tang et al., 2008).

Although the computational cost of WEMVA is significantly reduced, encoded simultaneous sources add crosstalk artifacts into the gradient. This becomes clear if

we express the encoded source and receiver wavefield as follows using the fact that wavefield propagation is linear with respect to sources:

$$\widetilde{S}(\mathbf{x},\omega)=\sum_{\mathbf{x}_s} S(\mathbf{x},\mathbf{x}_s,\omega)\alpha^*(\mathbf{x}_s,\omega), \tag{15}$$

and

$$\widetilde{R}(\mathbf{x},\omega)=\sum_{\mathbf{x}_s} R(\mathbf{x},\mathbf{x}_s,\omega)\alpha(\mathbf{x}_s,\omega). \tag{16}$$

Substituting equations 15 and 16 into 14 and using the fact that $\alpha^*(\mathbf{x}_s,\omega)\alpha(\mathbf{x}'_s,\omega)=1$ if $\mathbf{x}_s=\mathbf{x}'_s$ yield

$$\widetilde{g}(\mathbf{y})=g(\mathbf{y})+g_c(\mathbf{y}), \tag{17}$$

where g_c is the crosstalk:

$$g_c(\mathbf{y})=\sum_{\omega}\sum_{\mathbf{x}_s}\sum_{\mathbf{x}'_s\neq\mathbf{x}_s}\left(\frac{\partial S(\mathbf{x},\mathbf{x}_s,\omega)}{\partial v(\mathbf{y})}R(\mathbf{x},\mathbf{x}'_s,\omega)+S(\mathbf{x},\mathbf{x}_s,\omega)\frac{\partial R(\mathbf{x},\mathbf{x}'_s,\omega)}{\partial v(\mathbf{y})}\right)\times\alpha^*(\mathbf{x}_s,\omega)\alpha(\mathbf{x}'_s,\omega). \tag{18}$$

A way to mitigate the influence of crosstalk is to change the random encoding function at each iteration (Krebs et al., 2009), so that the crosstalk will be destructively stacked over WEMVA iterations and consequently converge to zero because it has a zero expectation. It is important to point out that regeneration of the random code will result in the objective function (equation 8) changing at each iteration. Therefore, the objective function may not be monotonically decreasing over iterations, as opposed to the case in conventional separate-source WEMVA. The optimization algorithm using encoded simultaneous sources is summarized in Algorithm 1.

Algorithm 1 Encoded simultaneous-source WEMVA algorithm

generate random code and assemble all shot gathers together
compute the migrated image: $\widetilde{\mathbf{m}}^0_{\text{mig}}$
compute the gradient: $\widetilde{\mathbf{g}}_0$
initialize the search direction: $\mathbf{p}_0=-\widetilde{\mathbf{g}}_0$
for $k=1\cdots N_k$ **do**
  perform line search: optimize λ, $\underset{\lambda}{\text{argmin}}\ \widetilde{J}(\mathbf{v}_{k-1}+\lambda\mathbf{p}_{k-1})$
  update the velocity model: $\mathbf{v}_k=\mathbf{v}_{k-1}+\lambda\mathbf{p}_{k-1}$
  generate random code and assemble all shot gathers together
  compute the migrated image: $\widetilde{\mathbf{m}}^k_{\text{mig}}$
  compute the gradient: $\widetilde{\mathbf{g}}_k$
  find the search direction: $\mathbf{p}_k=-\widetilde{\mathbf{g}}_k+\frac{(\widetilde{\mathbf{g}}_k)^T(\widetilde{\mathbf{g}}_k-\widetilde{\mathbf{g}}_{k-1})}{(\widetilde{\mathbf{g}}_{k-1})^T\widetilde{\mathbf{g}}_{k-1}}$
end for

NUMERICAL EXAMPLES

I apply the encoded simultaneous-source WEMVA on a truncated Marmousi model. The data used for inversion are generated using prestack Born wavefield modeling (Stolt and Benson, 1986; Tang, 2011). Hence the data only contain primary reflections and fit the theory perfectly. I use one-way wavefield extrapolation to carry out the numerical experiments. Since one-way wavefield extrapolation does not generate back scatterings, the velocity model used for Born modeling does not need to be smooth. Figures 1(a) and 1(b) show the velocity model and reflectivity model used for Born modeling. I use a Ricker wavelet with a dominant frequency of 15 Hz as the source function for modeling. The source function is assumed to be known in the subsequent inversion tests.

The initial velocity model used for inversion is shown in Figure 2. It is a smoothed version of the true velocity model (Figure 1(a)). The initial velocity model is accurate enough so that no cycle skipping occurs during inversion. The goal of the experiments shown here is to demonstrate that with an initial velocity model that guarantees the convergence of inversion, encoded simultaneous-source WEMVA produces similar inversion result as does conventional separate-source WEMVA, but with a significantly reduced computational cost. However, the convergence property using an initial velocity model far from the correct one still needs to be studied, and it remains an area for further investigation.

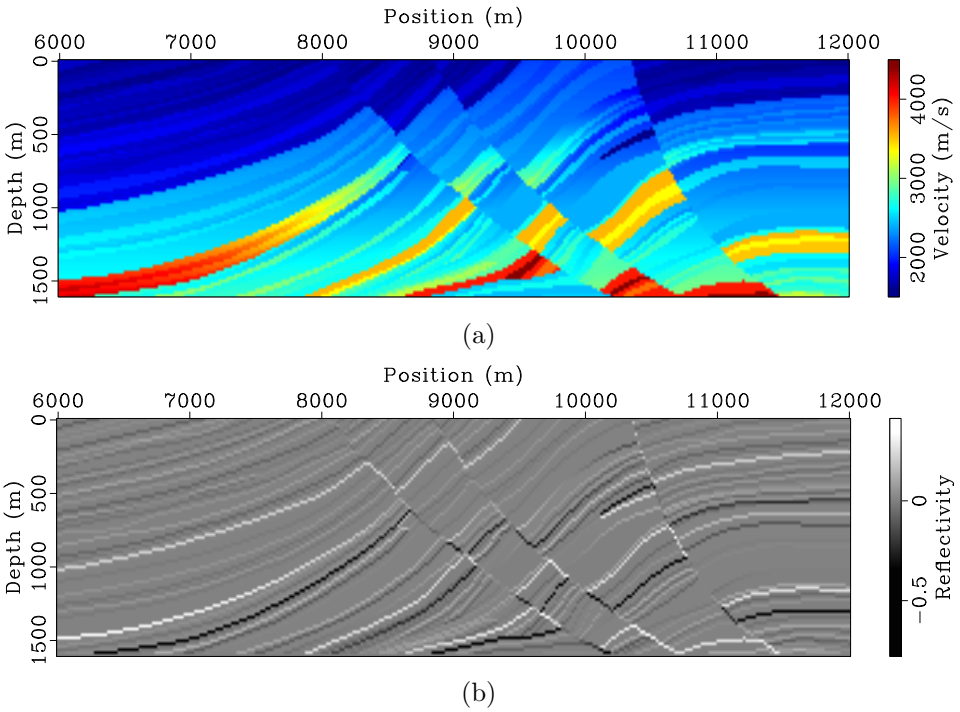

Figure 1: The velocity model (a) and reflectivity model (b) used for Born wavefield modeling. [**ER**]

I test the inversion on data sets acquired using both land and marine acquisition

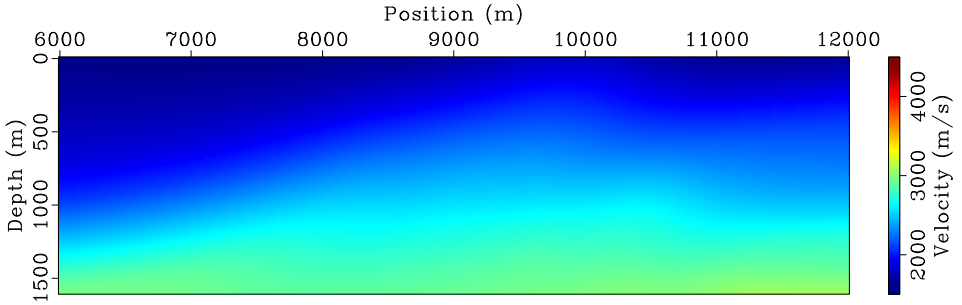

Figure 2: The initial velocity model. [**ER**]

geometries. The data acquired from a land acquisition geometry contains 101 shots ranging from 5 km to 13 km with a 80 m sampling interval. The receiver spread ranges from 5 km to 13 km and is fixed for all shots. The receiver sampling interval is 20 m. For the data acquired using a marine acquisition geometry, the 101 sources also range from 5 km to 13 km and sampled at 80 m. The minimum and maximum offsets for each shot is 0 and 6 km. The receiver sampling interval is also 20 m.

I run inversion using both separate sources and encoded simultaneous sources after the same number of iterations. Figures 3 and 4 compare the WEMVA gradients at the first iteration for different methods and different acquisition geometries. Note the randomized crosstalk present in the simultaneous-source WEMVA gradients. Because I regenerate the random code at the beginning of each iteration, the crosstalk is expected to be incoherently stacked over iterations. Therefore, the impact of crosstalk will be mitigated.

Figures 5 and 6 show the separate-source inversion results at different iterations for land and marine acquisition geometries, respectively. The velocity model has been successfully recovered in both cases. But inversion using land acquisition geometry produces a slightly better final inversion result (Figure 5(d)) than the one obtained using marine acquisition geometry (Figure 6(d)). This is because, for this particular example, the land acquisition geometry has wider offsets and hence gives better coverage to the model.

For comparison, Figures 7 and 8 present the encoded simultaneous-source inversion results for land and marine acquisition geometries, respectively. As expected, the inverted velocity model at early iterations (Figures 7(a) and 7(b) for land acquisition geometry and Figures 8(a) and 8(b) for marine acquisition geometry) have been strongly affected by the crosstalk artifacts in the gradients (Figure 4). As inversion proceeds, the crosstalk artifacts are destructively stacked, and hence the influence of crosstalk is decreasing over iterations. The final inversion results (Figures 7(d) and 8(d)) also successfully recover the velocity model. However, the encoded simultaneous-source WEMVA seems to be more sensitive to the model coverage, and the convergence of inversion using the data acquired with a marine geometry (Figure 8(d)) is considerably slower than that obtained using the data acquired from a land

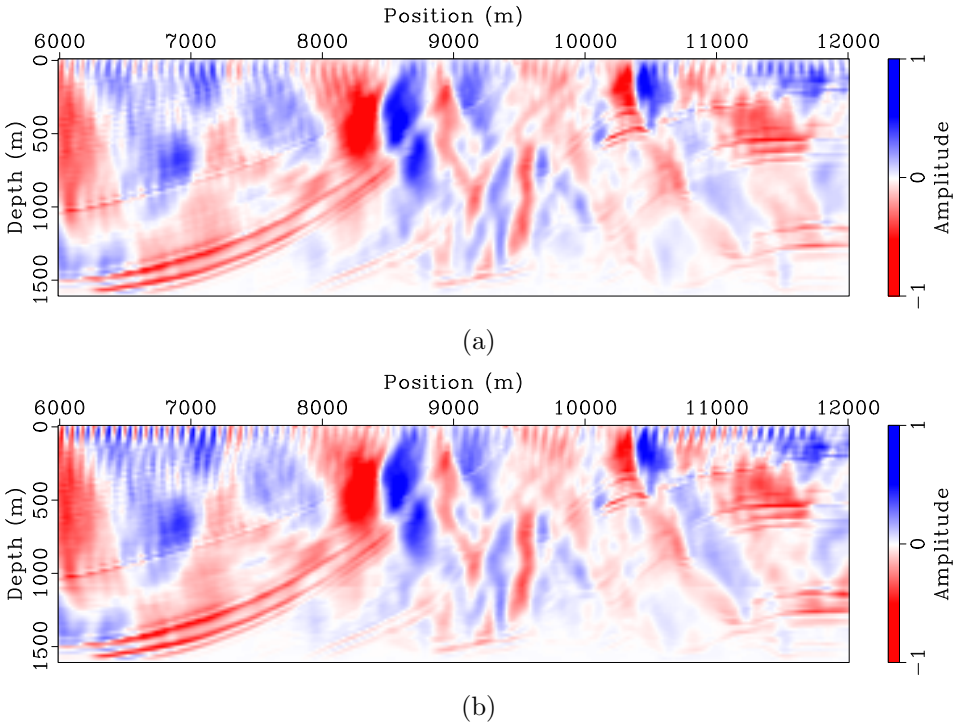

Figure 3: Gradient of separate-source WEMVA at the first iteration for (a) land acquisition geometry and (b) marine acquisition geometry. [**ER**]

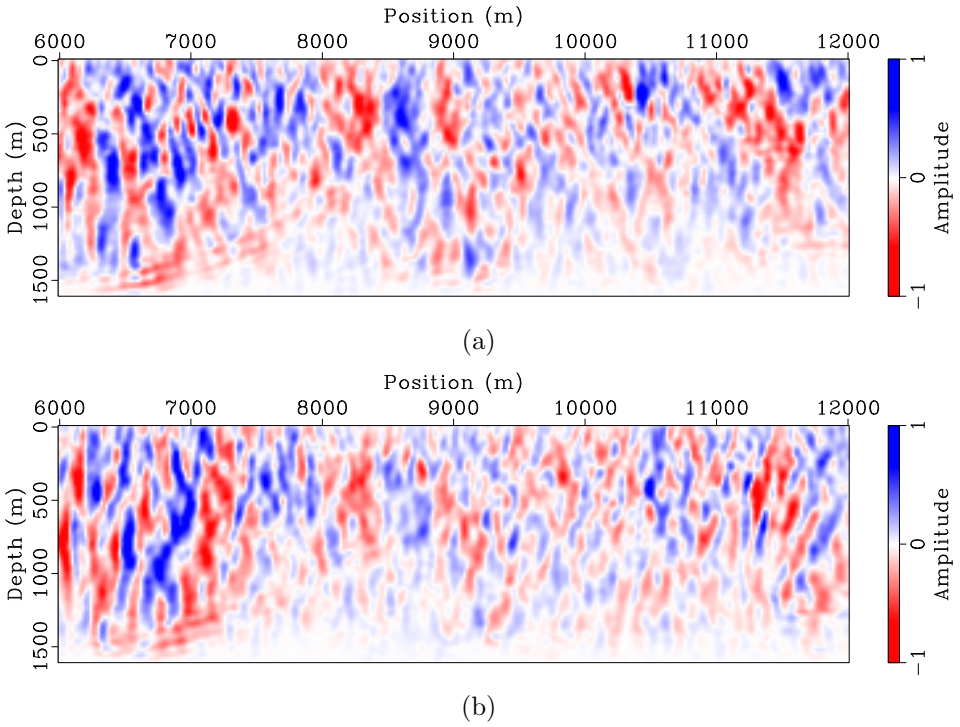

Figure 4: Gradient of encoded simultaneous-source WEMVA at the first iteration for (a) land acquisition geometry and (b) marine acquisition geometry. [**ER**]

acquisition geometry (Figure 7(d)).

As a further comparison of the convergence, Figure 9 shows the data misfit (the objective function) obtained using different methods and for different acquisition geometries. The data misfit curve for each case has been normalized with its value at the first iteration. Note that the data misfit functions decrease monotonically for separate-source inversions. This is because the objective function J is consistent over iterations, and therefore the nonlinear conjugate gradient algorithm tries to minimize the same objective function over iterations. In contrast, the data misfit functions for encoded simultaneous-source inversions fluctuate significantly, and they do not show monotonically decreasing behavior as do separate-source inversions. This is because the random phase encoding function keeps changing at each iteration, and consequently the objective function $\widetilde{J}$ varies over iterations. The nonlinear conjugate gradient algorithm cannot guarantee the monotonic decrease of the objective function. But the misfit functions do show an overall decreasing trend.

Since this is a synthetic-data example, the true velocity model is known. I calculate the model misfit in ℓ_2 norm and the results are plotted in Figure 10. It is interesting to note that although encoded simultaneous-source inversion does not show monotonic decrease of the data misfit, it does show monotonic decrease of the model misfit, which suggests that the inversion is going in the correct direction. Also note that the model convergence of encoded simultaneous-source inversion is slower than that of separate-source inversion. The difference seems to be insignificant for land acquisition geometries, where the receivers are fixed and the offsets are longer. The difference for marine acquisition geometries, however, is much bigger. This is probably because the marine acquisition geometry used in this example has shorter offsets and the data coverage is much less than the land acquisition geometry. The lack of data coverage may require more iterations to remove the crosstalk artifacts. This speculation, however, still needs more investigation to verify.

A final comparison is made among the images obtained using the inverted velocity model produced by different methods and for different acquisition geometries. The initial images (Figure 11) show poor focusing due to the velocity errors. The updated images using velocities obtained with separate sources (Figure 13) and encoded simultaneous sources (Figure 13) show significantly improvements on image focusing and coherence. The updated images using both separate-source inversion and encoded simultaneous-source inversion show very similar overall qualities, although separate-source inversion does produces slightly better images. But if we take the cost into account, the encoded simultaneous-source inversion is about 101 times faster than the separate-source inversion, which is a significant advantage. For comparison, Figure 14 presents images obtained using the true velocity model (Figure 1(a)).

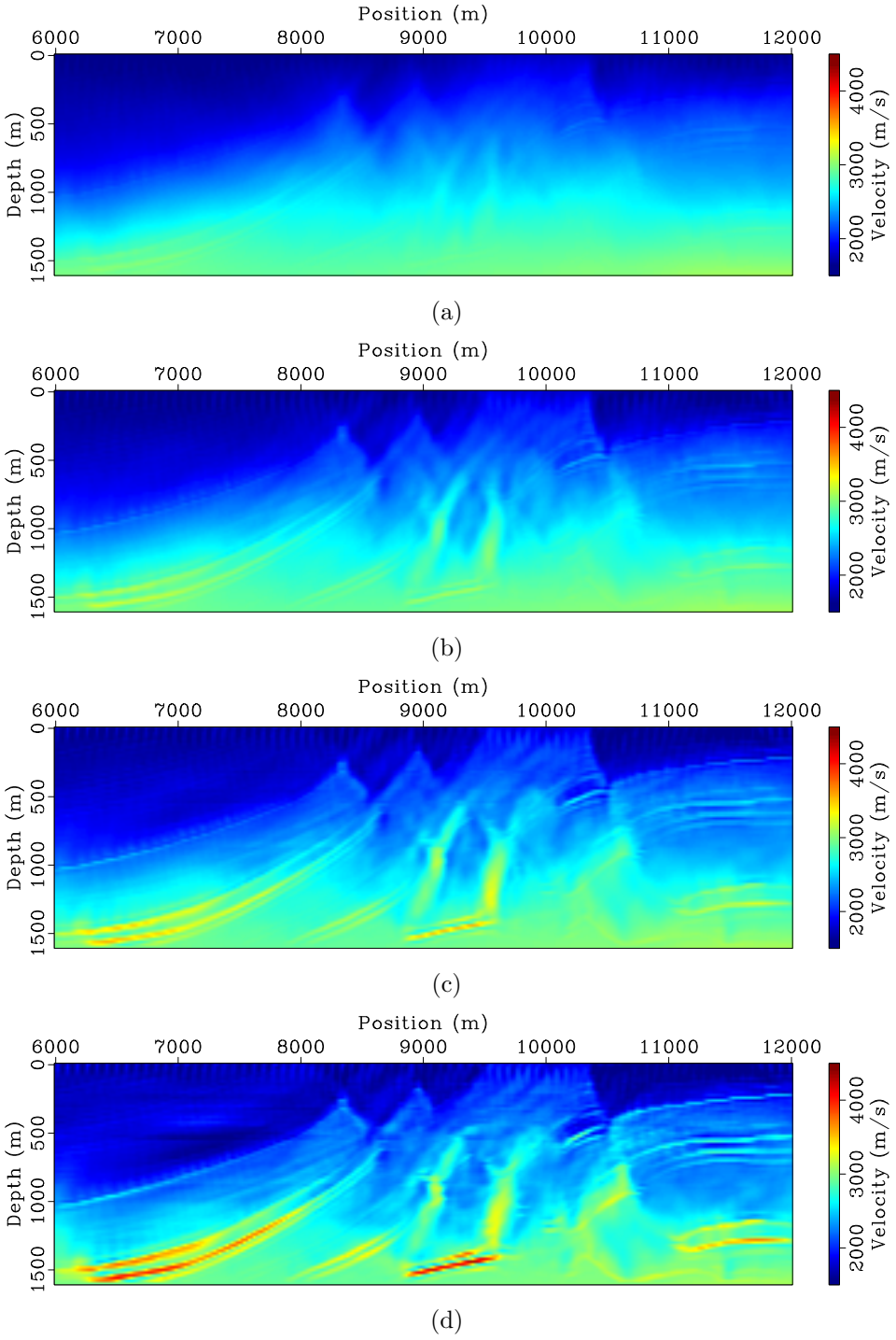

Figure 5: Separate-source WEMVA inversion result for land acquisition geometry at (a) 5, (b) 20, (c) 50 and (d) 120 iterations, respectively. [**CR**]

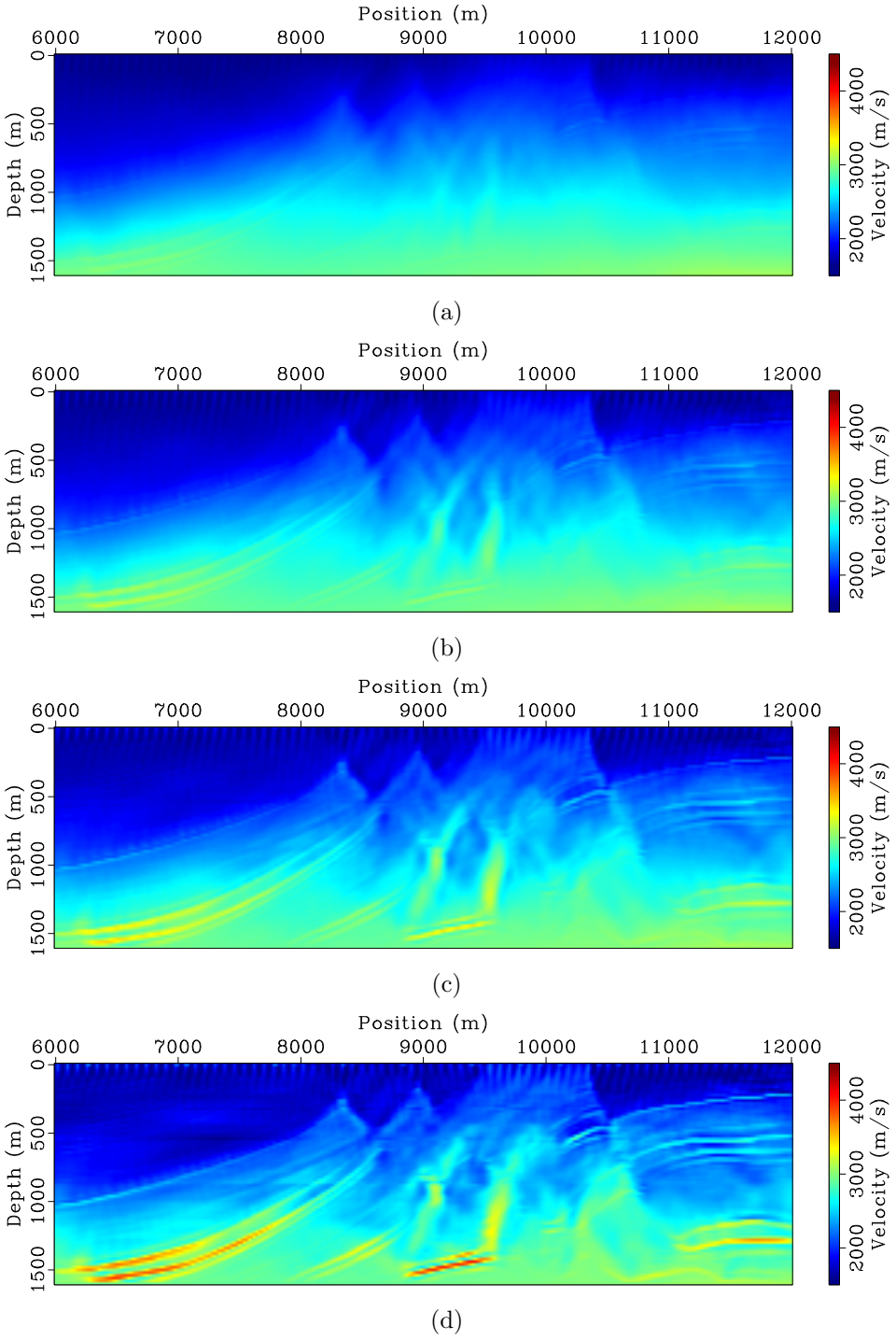

Figure 6: Separate-source WEMVA inversion result for marine acquisition geometry at (a) 5, (b) 20, (c) 50 and (d) 120 iterations, respectively. [**CR**]

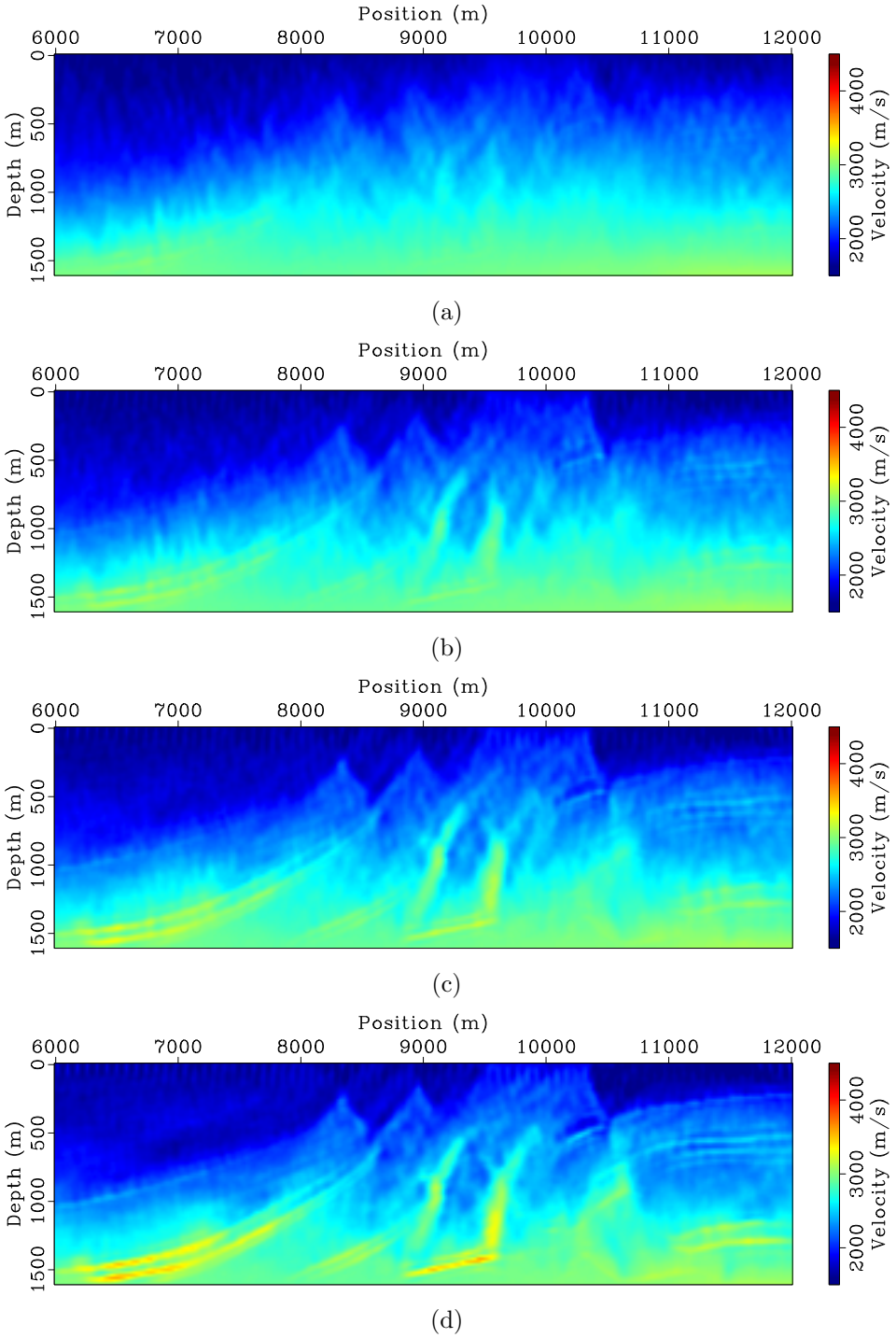

Figure 7: Encoded simultaneous-source WEMVA inversion result for land acquisition geometry at (a) 5, (b) 20, (c) 50 and (d) 120 iterations, respectively. [**ER**]

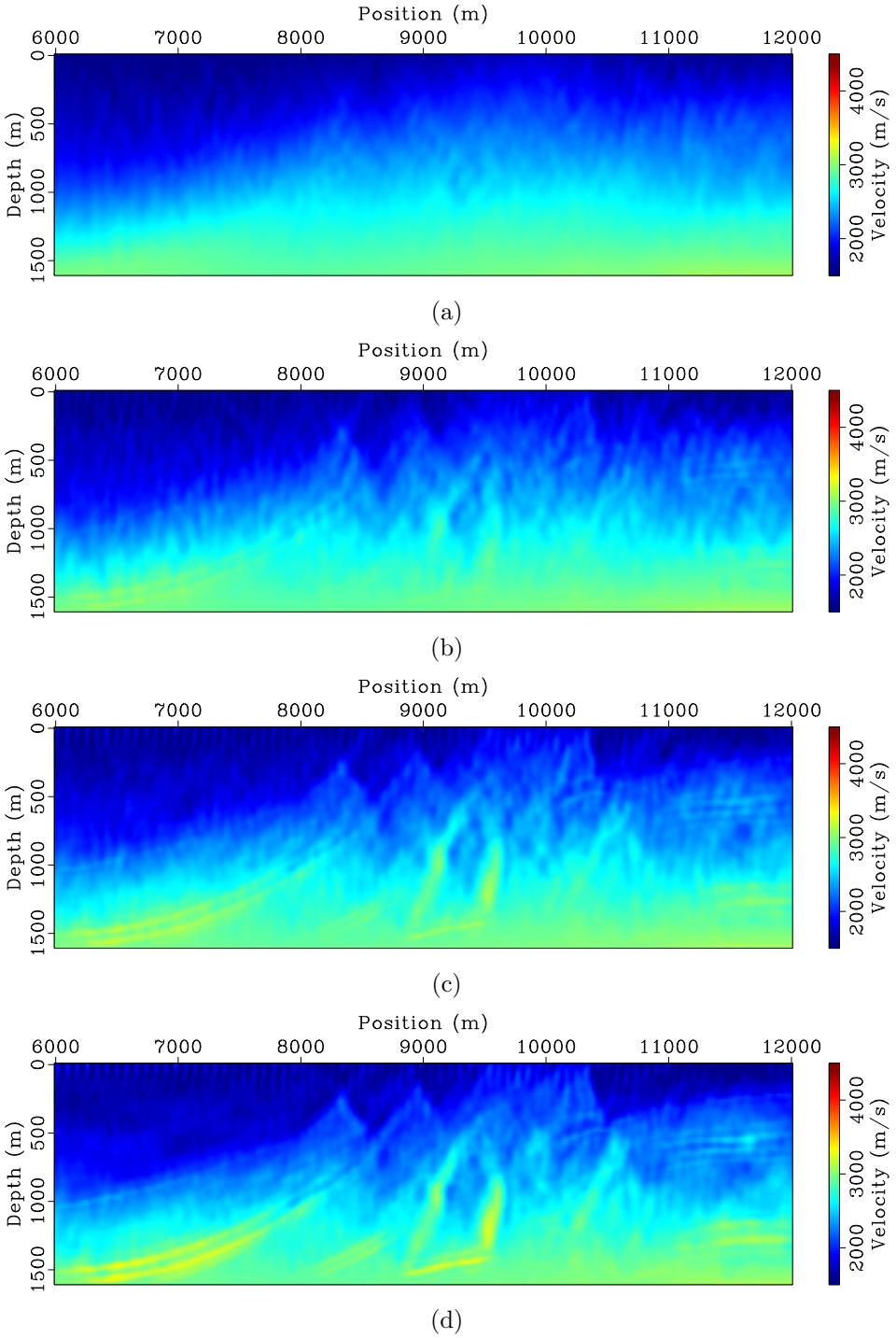

Figure 8: Encoded simultaneous-source WEMVA inversion result for marine acquisition geometry at (a) 5, (b) 20, (c) 50 and (d) 120 iterations, respectively. [**ER**]

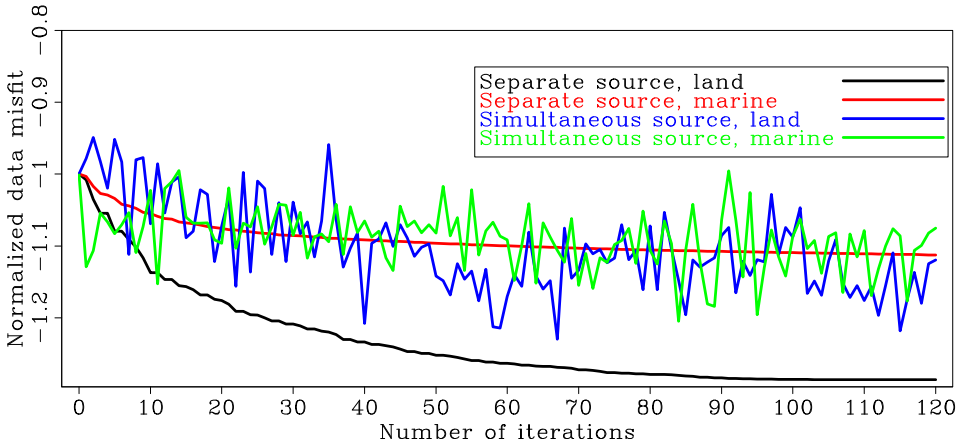

Figure 9: Normalized data misfit as a function of iterations for different methods. [**CR**]

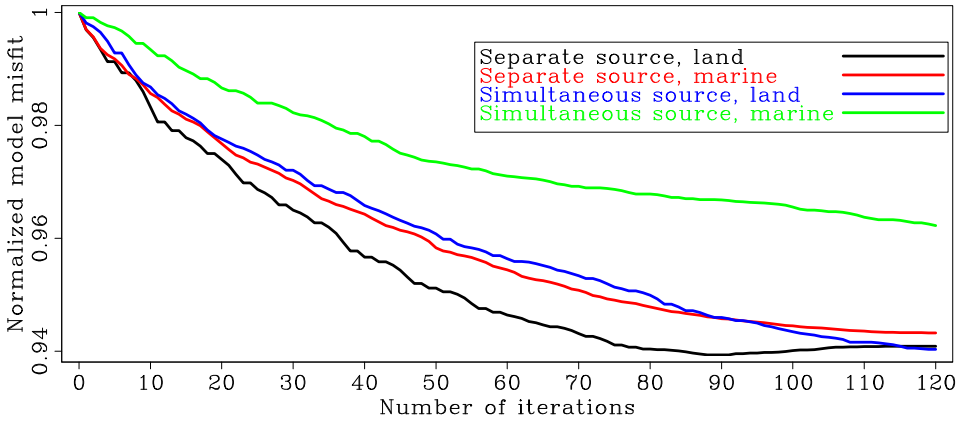

Figure 10: Normalized model misfit as a function of iterations for different methods. [**CR**]

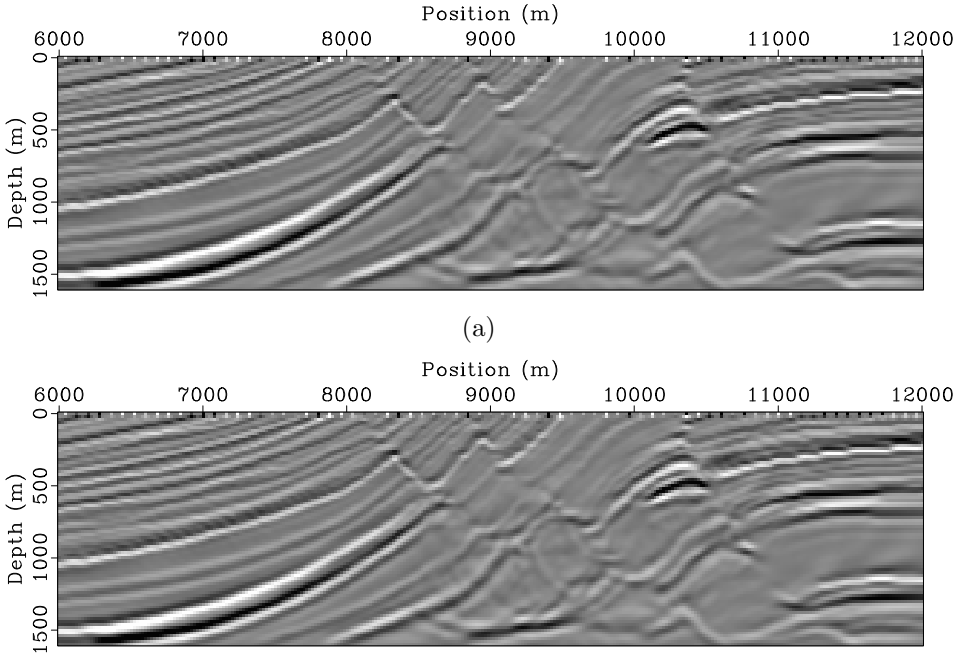

Figure 11: Image obtained using the initial velocity model (Figure 2) for (a) land acquisition geometry and (b) marine acquisition geometry. [**ER**]

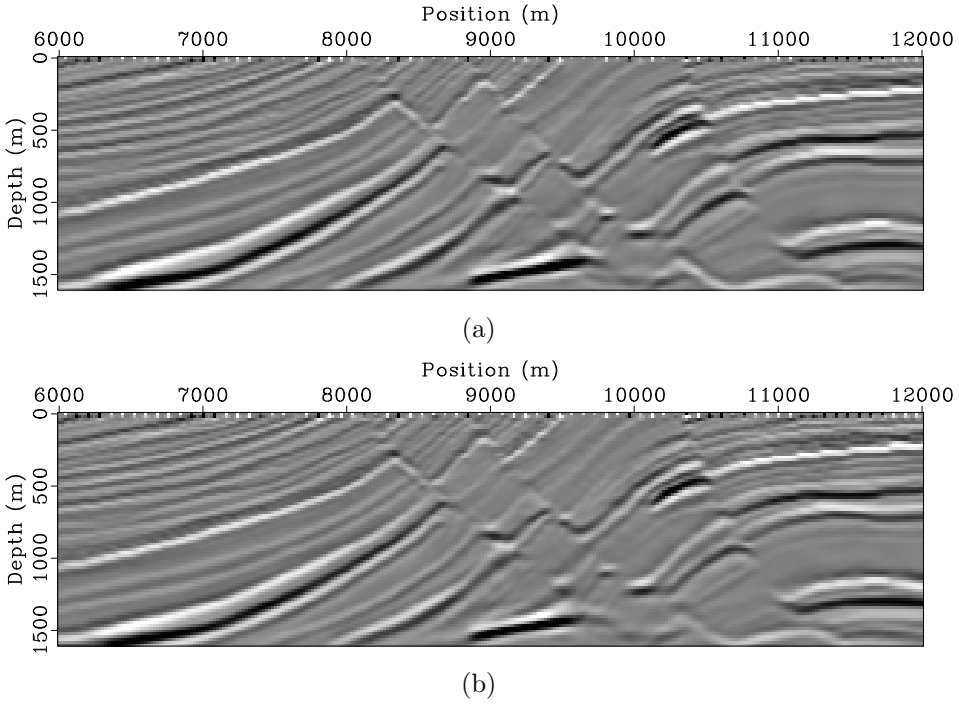

Figure 12: Image obtained using the separate-source inverted velocity model for (a) land acquisition geometry and (b) marine acquisition geometry. [**CR**]

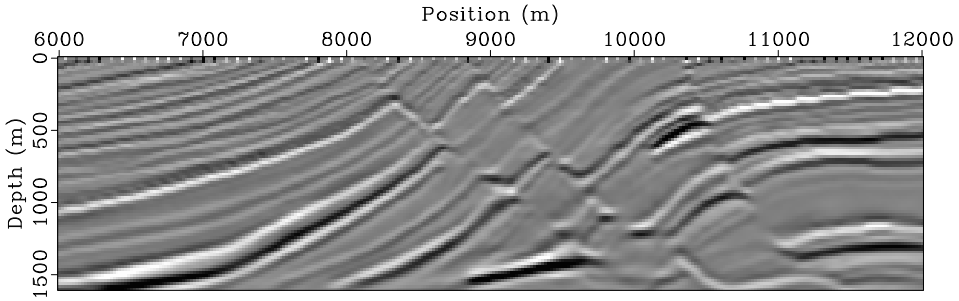

(a)

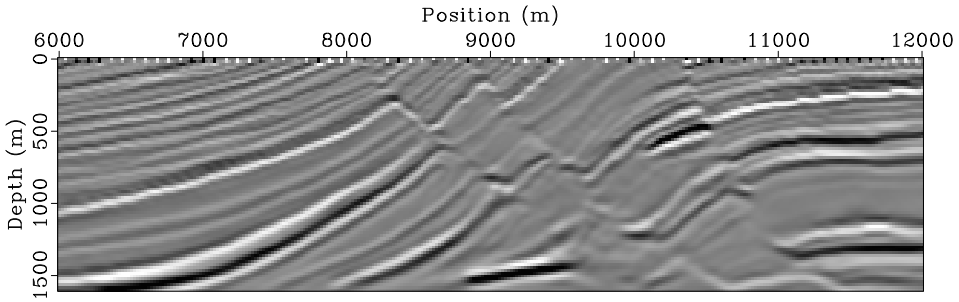

(b)

Figure 13: Image obtained using the encoded simultaneous-source inverted velocity model for (a) land acquisition geometry and (b) marine acquisition geometry. [**ER**]

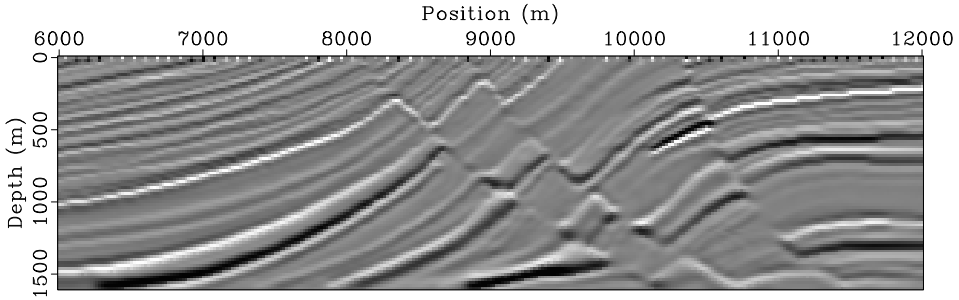

(a)

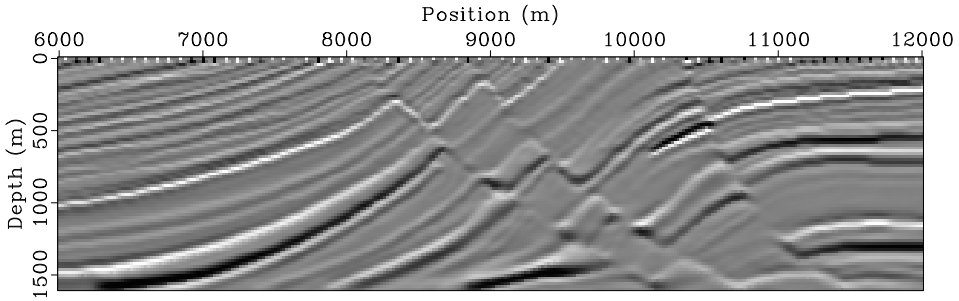

(b)

Figure 14: Image obtained using the true velocity model (Figure 1(a)) for (a) land acquisition geometry and (b) marine acquisition geometry. [**ER**]

CONCLUSIONS

I have presented an efficient method for velocity optimization using wavefields. The method is automatic because it maximizes the image stack power (or minimizes its negative) and no picking is necessary. The method is extremely fast because it assembles all shot gathers together and migrates them at once, instead of migrating them separately. The shot gathers need to be reassembled with regeneration of random phase-encoding functions at each iteration to mitigate the impact of crosstalk present in the gradient. The encoding strategy can be applied to both land and marine acquisition geometries, regardless of whether or not a fixed receiver spread has been used. Numerical examples demonstrate that encoded simultaneous-source inversion gives reasonably good recovery of the velocity model, with the advantage that the computational cost is independent from the number of sources.

REFERENCES

Albertin, U., P. Sava, J. Etgen, and M. Maharramov, 2006, Adjoint wave-equation velocity analysis: SEG Technical Program Expanded Abstracts, **25**, 3345–3349.

Beasley, C. J., 2008, A new look at marine simultaneous sources: The Leading Edge, **27**, 914–917.

Beasley, C. J., R. E. Chambers, and Z. Jiang, 1998, A new look at simultaneous sources: SEG Technical Program Expanded Abstracts, **17**, 133–135.

Ben-Hadj-Ali, H., S. Operto, and J. Virieux, 2011, An efficient frequency-domain full waveform inversion method using simultaneous encoded sources: Geophysics, **76**, R109–R124.

Berkhout, A. J. G., 2008, Changing the mindset in seismic data acquisition: The Leading Edge, **27**, 924–938.

Biondi, B. and P. Sava, 1999, Wave-equation migration velocity analysis: SEG Technical Program Expanded Abstracts, **18**, 1723–1726.

Dai, W., C. Boonyasiriwat, and G. T. Schuster, 2010, 3D multi-source least-squares reverse time migration: SEG Technical Program Expanded Abstracts, **29**, 3120–3124.

Dai, W. and J. Schuster, 2009, Least-squares migration of simultaneous sources data with a deblurring filter: SEG Technical Program Expanded Abstracts, **28**, 2990–2994.

Fei, W., P. Williamson, and A. Khoury, 2009, 3-D common-azimuth wave-equation migration velocity analysis: SEG Technical Program Expanded Abstracts, **28**, 2283–2287.

Hampson, G., J. Stefani, and F. Herkenhoff, 2008, Acquisition using simultaneous sources: The Leading Edge, **27**, 918–923.

Krebs, J. R., J. E. Anderson, D. Hinkley, R. Neelamani, S. Lee, A. Baumstein, and M.-D. Lacasse, 2009, Fast full-wavefield seismic inversion using encoded sources: Geophysics, **74**, WCC177–WCC188.

Liu, F., D. W. Hanson, N. D. Whitmore, R. S. Day, and R. H. Stolt, 2006, Toward a unified analysis for source plane-wave migration: Geophysics, **71**, no. 4, S129–S139.

Romero, L. A., D. C. Ghiglia, C. C. Ober, and S. A. Morton, 2000, Phase encoding of shot records in prestack migration: Geophysics, **65**, 426–436.

Sava, P. and I. Vlad, 2008, Numeric implementation of wave-equation migration velocity analysis operators: Geophysics, **73**, VE145–VE159.

Shen, P., 2004, Wave-equation migration velocity analysis by differential semblance optimization: PhD thesis, Rice University.

Shen, P., W. W. Symes, S. Morton, A. Hess, and H. Calandra, 2005, Differential semblance velocity analysis via shot profile migration: SEG Technical Program Expanded Abstracts, **24**, 2249–2252.

Soubaras, R. and B. Gratacos, 2007, Velocity model building by semblance maximization of modulated-shot gathers: Geophysics, **72**, U67–U73.

Stolt, R. H. and A. Benson, 1986, Seismic migration: Theory and practice: Geophysical Press.

Tang, Y., 2011, Imaging and velocity analysis by target-oriented wavefield inversion: PhD thesis, Stanford University.

Tang, Y. and B. Biondi, 2009, Least-squares migration/inversion of blended data: SEG Technical Program Expanded Abstracts, **28**, 2859–2863.

Tang, Y., C. Guerra, and B. Biondi, 2008, Image-space wave-equation tomography in the generalized source domain: **SEP-136**, 1–22.

Tang, Y. and S. Lee, 2010, Preconditioning full waveform inversion with phase-encoded Hessian: SEG Technical Program Expanded Abstracts, **29**, 1034–1038.

Whitmore, N. D., 1995, An imaging hierarchy for common angle plane wave seismogram: PhD thesis, University of Tulsa.

Zhang, Y., J. Sun, C. Notfors, S. H. Gray, L. Chernis, and J. Young, 2005, Delayed-shot 3D depth migration: Geophysics, **70**, E21–E28.

APPENDIX A

EQUIVALENCE OF IMAGE-STACK-POWER MAXIMIZATION AND DATA-DOMAIN BORN WAVEFIELD INVERSION

This appendix shows that maximizing the image stack power (or minimizing its negative) is equivalent to Born wavefield inversion, which minimizes the difference between the modeled and observed primaries. The difference-based objective function for data-domain Born wavefield inversion can be defined as follows:

$$J = \frac{1}{2}(\mathbf{Lm} - \mathbf{d}_{\text{obs}})^*(\mathbf{Lm} - \mathbf{d}_{\text{obs}}), \tag{A-1}$$

where $\mathbf{d}_{\text{obs}}$ is the observed data vector, $\mathbf{m}$ is the reflectivity vector; $\mathbf{L}$ is the Born modeling operator that only modeled the angle stacked reflectivity (zero-subsurface-

offset reflectivity), which is a function of the velocity vector $\mathbf{v}$. Objective function A-1 is minimized by optimizing both $\mathbf{v}$ and $\mathbf{m}$. Expanding equation A-1 yields

$$J = \frac{1}{2}\left(\mathbf{m}^*\mathbf{L}^*\mathbf{L}\mathbf{m} - \mathbf{m}^*\mathbf{L}^*\mathbf{d}_{\rm obs} - \mathbf{d}_{\rm obs}^*\mathbf{L}\mathbf{m} + \mathbf{d}_{\rm obs}^*\mathbf{d}_{\rm obs}\right). \tag{A-2}$$

In the least-squares sense, the reflectivity model $\mathbf{m}$ can be formally obtained as follows, assuming the Hessian $\mathbf{H}$ is invertible:

$$\mathbf{m} = (\mathbf{L}^*\mathbf{L})^{-1}\mathbf{L}^*\mathbf{d}_{\rm obs} = \mathbf{H}^{-1}\mathbf{L}^*\mathbf{d}_{\rm obs}. \tag{A-3}$$

Substituting equations A-3 into A-2 and simplifying yield

$$J = \frac{1}{2}\left(-\mathbf{d}_{\rm obs}^*\mathbf{L}\mathbf{H}^{-1}\mathbf{L}^*\mathbf{d}_{\rm obs} + \mathbf{d}_{\rm obs}^*\mathbf{d}_{\rm obs}\right) \tag{A-4}$$

Since $\mathbf{d}_{\rm obs}^*\mathbf{d}_{\rm obs}$ is a constant, it can be ignored in the above equation, therefore

$$J \approx -\frac{1}{2}\mathbf{d}_{\rm obs}^*\mathbf{L}\mathbf{H}^{-1}\mathbf{L}^*\mathbf{d}_{\rm obs}. \tag{A-5}$$

Note that the migration image $\mathbf{m}_{\rm mig}$ is defined as follows:

$$\mathbf{m}_{\rm mig} = \mathbf{L}^*\mathbf{d}_{\rm obs}. \tag{A-6}$$

Substituting equations A-6 into A-5 yields

$$J \approx -\frac{1}{2}\mathbf{m}_{\rm mig}^*\mathbf{H}^{-1}\mathbf{m}_{\rm mig}. \tag{A-7}$$

To simplify the problem, I ignore the Hessian $\mathbf{H}$ in equation A-7 and assume it to be an identity matrix. Therefore, equation A-7 becomes

$$J \approx -\frac{1}{2}\mathbf{m}_{\rm mig}^*\mathbf{m}_{\rm mig}, \tag{A-8}$$

which is the same as equation 1 defined in the body of the paper. However, the Hessian $\mathbf{H}$ in equation A-7 might be important, especially in complex geologies, where the illumination is distorted by complex overburdens. The importance of the Hessian in equation A-7 remains an area for further investigation.